

CAROS-Q: Climbing Aerial RObot System Adopting Rotor Offset With a Quasi-Decoupling Controller

Hyungyu Lee^{ID}, Byeongho Yu, Christian Tirtawardhana, Chanyoung Kim, Myeongwoo Jeong,
Sumin Hu, and Hyun Myung^{ID}, *Senior Member, IEEE*

Abstract—Unmanned Aerial Vehicles (UAVs) have continually proven their effectiveness in various fields. However, UAVs have not yet matured enough to be used for vertical surface maintenance tasks, such as building inspection or cleaning. To mitigate this issue, this letter proposes a novel design for a coaxial hexarotor (Y6) with a tilting mechanism that can morph midair while in a hover, changing the flight stage from a horizontal to a vertical orientation, and vice versa, thus allowing wall-perching and wall-climbing maneuvers. Furthermore, a rotor offset design has been adopted, in which the tilting rotors are offset from the tilting axle by a certain distance. In this configuration, the required distance between the wall and the platform is reduced, improving stability and increasing the opportunity to enhance power efficiency. However, owing to the rotor offset, the servo motor slows down and the tilting angle is one-way constrained. These conditions can cause a critical issue with the conventional control method. To tackle the problem, a novel control method called quasi-decoupling control is proposed. Our proposed method attains promising performance, overcoming the limitations of a servo motor’s slow dynamics and angular constraint.

Index Terms—Aerial systems: applications, aerial systems: mechanics and control.

I. INTRODUCTION

IN RECENT years, through numerous and diverse researches, robots have become evermore capable as human substitutes in many different tasks in a wide variety of fields [1], [2]. In spite of this rapid development of robots, humans are still exposed to potential dangers in some areas of application, such as those associated with the maintenance of massive structures (e.g., skyscrapers and bridges) that require constant cleaning and inspection, which involve direct interaction with the exterior wall. A common method is to use permanent gondola systems. However, these are inefficient, considering the installation on a

Manuscript received June 14, 2021; accepted August 5, 2021. Date of publication August 30, 2021; date of current version September 16, 2021. This letter was recommended for publication by Associate Editor M. Bangura and Editor P. Pounds upon evaluation of the reviewers’ comments. This was supported by the National Research Foundation of Korea (NRF) Grant funded by the Ministry of Science and ICT for First-Mover Program for Accelerating Disruptive Technology Development (NRF-2018M3C1B9088328). The students are supported by BK21 FOUR. (*Corresponding author: Hyun Myung.*)

Hyungyu Lee, Byeongho Yu, Christian Tirtawardhana, Sumin Hu, and Hyun Myung are with the School of Electrical Engineering, Korea Advanced Institute of Science and Technology (KAIST), Daejeon 34141, Republic of Korea (e-mail: lshoon93@kaist.ac.kr; bhyu@kaist.ac.kr; christiant@kaist.ac.kr; 2minus1@kaist.ac.kr; hmyung@kaist.ac.kr).

Chanyoung Kim and Myeongwoo Jeong are with the Urban Robotics Laboratory, KAIST, Daejeon 34141, Republic of Korea (e-mail: slowtuttle99@kaist.ac.kr; wjdaudnn147@kaist.ac.kr).

Digital Object Identifier 10.1109/LRA.2021.3108489

fixed position, and become pointless on discontinuous building surfaces.

To resolve this challenge, several researchers have developed wall-climbing robots [3], [4]. Owing to the dependency on wires or wall-sticking mechanisms, these inventions, however, have difficulties overcoming gaps and obstacles, are easily affected by the condition of the contact surface, and are relatively time-consuming to use. Contrarily, using UAVs for wall interaction work on a massive structure is an exemplary substitution for human tasks, thus eradicating the need for human labor in extreme conditions, as well as being very cost-effective. Therefore, these benefits make wall-climbing, which enables wall interaction, with UAVs an attractive research field.

There are various types of multirotor UAVs with wall-climbing capabilities. Some multirotor UAVs are equipped with additional mechanisms for climbing, such as take-off arms and light actuated hook-shaped feet in [5] and active rubber wheels in [6]. However, those climbing methods still rely on the surface condition. The other approach is to equip UAVs with an actuated arm, designed to interact directly with the surface, without wall-climbing [7], [8]. While in flight, the platform must keep some distance from the wall to prevent collision. In this situation, the end effector must interact with the wall, thus it must reach the wall at the farthest point from the UAV’s center of gravity (CoG). This results in an asymmetric mass distribution that affects flight stability, which is a focus analyzed in this letter.

Another noticeable approach is employing fully-actuated multirotor systems using tilting propellers [9]–[14]. In [9], modeling and simulation of a quadrotor with tilting rotors were presented, and the platform was experimentally tested in [10]. A fully actuated quadrotor design was proposed in [11] and a hexarotor-based method, utilizing only a servo motor, was evaluated in [12]. While improving maneuverability, these approaches did not show a large attitude-changing capability, such as over 30°, which is essential for wall-climbing tasks. There have been approaches that can perform 90° attitude change by pairing each rotor with a servo motor, based on a quadrotor [13] and a hexarotor [14]. These UAVs can approach walls even closer than those without the tilting mechanism; however, they cannot approach the walls closer than the propeller’s radius. Furthermore, they require assumptions that the servo motor dynamics are fast enough, and the servo motor’s angle should not be constrained in one way. Additionally, the platform, which already has some payload limitations, must endure the additional weight of the servo motors paired with rotors.

In this letter, we propose CAROS-Q, which stands for a Climbing Aerial RObot System adopting rotor offset with Quasi-decoupling controller. CAROS-Q is a novel tiltable coaxial hexacopter that overcomes the aforementioned limitations of

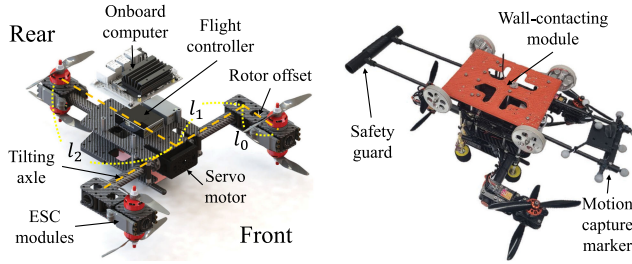


Fig. 1. The 3D CAD drawing (left) and prototype (right) of the proposed CAROS-Q.

the conventional approaches. The contribution of this letter is threefold:

- We propose CAROS-Q, an optimized tilting coaxial hexarotor for wall-perching and wall-climbing situations in which the additional mechanism, such as a wall-contacting mechanism, should be installed. CAROS-Q improves stability and increases the opportunity to enhance power efficiency while wall-perching and wall-climbing by deliberately positioning the rotors a certain distance away from the tilting axle, which is called rotor offset.
- To the best of our knowledge, CAROS-Q is the first successful attempt of a tilting multirotor that can perform midair pitching with a maximum of 90° and wall-climbing with only a servo motor. The tilting mechanism of CAROS-Q is actuated by only a servo motor, which reduces the payload and yields advantages in control.
- We present a novel control method, called a quasi-decoupling control, which overcomes the servo motor's slow dynamics and angular constraint. The rotor offset slows down the tilting speed and limits the angle of the servo motor. These constraints by the rotor offset have been resolved through the quasi-decoupling control.

This letter is structured as follows. Section II describes the design of CAROS-Q and Section III explains the CAROS-Q's modeling. Section IV proposes the newly designed controller for CAROS-Q. Lastly, Section V demonstrates that the proposed controller works as designed through indoor experiments and conclusions are drawn in Section VI.

II. DESIGN

A. Design Considerations

In [14], the authors use conventional hexarotors because they have a simple structure relative to the number of rotors, in addition to the ability to generate sufficient thrust. Their fast tilting mechanism uses six servo motors, one for each rotor. However, six servo motors will burden the multirotor. For this reason, CAROS-Q adopts the Y6 configuration, which uses only a single servo for the tilting mechanism. The benefits of this design are threefold. First, two-thirds of the total thrust is controllable with only a single servo motor. Second, with just one servo motor, the control becomes efficient, which shall be described in Section IV. Third, the gyroscopic effect can be neglected in the Y6 configuration. Therefore, as shown in Fig. 1, we adopt the Y6 configuration design with a single tilttable axle.

Additionally, mounting the platform with a wall-contacting module became our first choice for design. However, with a conventional multirotor, to make contact with a vertical surface,

the mechanical arm has to reach out farther past the propeller radius because the end-effector has to make contact with the vertical surface. Thus, a multirotor with a mounted arm must achieve stable flight, even in conditions of asymmetrical mass distribution owing to the out-reaching arm.

To maintain a stable flight, the thrust difference between the front propellers and the rear propellers should be minimized, as follows:

$$\min_L \|\mathbf{T}_{\text{front}} - \mathbf{T}_{\text{rear}}\|^2 \quad (1)$$

where L is the distance from the CoG of the platform to the CoG of the wall-contacting module, $\mathbf{T}_{\text{front}}$ the thrust vector of the front propeller pair, \mathbf{T}_{rear} the thrust vector of the rear propeller pair, and $\|\cdot\|$ the L_2 norm. Note that the front and rear sides are specified in Fig. 1. To simplify the calculation, we assume that the circular boundaries of the adjacent propellers are tangential to each other. Thus, the force and moment equilibrium of a hexarotor system can be calculated as follows:

$$\begin{aligned} \mathbf{F}_z^B : & -\|\mathbf{T}_{\text{rear}}\| - 2\|\mathbf{T}_{\text{front}}\| + m_{\text{plat}}\|\mathbf{g}\| \\ & + m_{\text{mod}}\|\mathbf{g}\| = 0 \\ \mathbf{M}_y^B : & \frac{2\sqrt{3}}{3}\|\mathbf{T}_{\text{rear}}\|R_{\text{prop}} - \frac{2\sqrt{3}}{3}\|\mathbf{T}_{\text{front}}\|R_{\text{prop}} \\ & + m_{\text{mod}}\|\mathbf{g}\|L = 0 \end{aligned} \quad (2)$$

where \mathbf{F}_z^B is the force along the z -axis and \mathbf{M}_y^B the moment about the y -axis, both represented in the body frame, m_{plat} the mass of the platform, R_{prop} the radius of the propeller, m_{mod} the mass of the wall-contacting module, and \mathbf{g} the gravity vector. By solving (2), (1) can be rewritten as follows:

$$\min_L \|\mathbf{T}_{\text{front}} - \mathbf{T}_{\text{rear}}\|^2 = \left\| \frac{3\sqrt{3}m_{\text{mod}}\mathbf{g}}{2R_{\text{prop}}} L \right\|^2. \quad (3)$$

It is obvious that the minimum of (1) can be obtained when $L = 0$. However, the required dimension of rotating propellers constrains the minimum L depending on the configuration of the platform. In other words, in the case where the contact point is on the front part of the platform, the module has to be at least $\frac{3+\sqrt{3}}{3}R_{\text{prop}}$ away from the platform's CoG. This imbalance manifests unwanted torque to the platform, creating instability unlike a module mounted on top of the platform. Instead of trying to mount an out-reaching arm, which risks the stability of the platform, we place the contacting mechanism at the center of the platform. Then, we can implement a wall-perching process to perform vertical wall climbing during the contacting operation.

Another crucial aspect that needs to be considered in the design can be observed in Fig. 2. During the wall-climbing process, to avoid any collision owing to the tilting rotors, an adequate amount of space between the propellers and the wall should be secured. As a result, the wall-contacting module has to be located at a certain distance from the platform's CoG, which results in a negative effect on the stability. Fig. 2 shows the comparison of the distance between the platform's CoG and the wall in various configurations. The minimum distance D_{min} is determined by the platform shape and the propeller size. Fig. 2(a), which represents the case of a typical multirotor with a manipulator, shows D_{min} is almost as large as the propeller diameter. The optimal condition described in (3) can be achieved by employing a tilting axle with the rotor offset and performing pose-changing, as shown in Fig. 2(c).

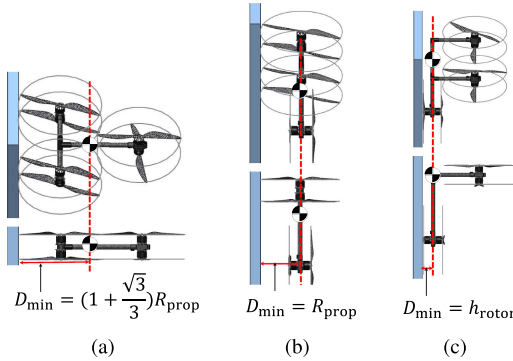


Fig. 2. A minimum distance between the CoG of the platform and the wall according to configurations. (a) The configuration of the general Y6 without a tilting mechanism, (b) a general tilting Y6 without the rotor offset, and (c) CAROS-Q, a tilting Y6 with the rotor offset.

In the case of the tilting multirotors without the rotor offset [14], D_{\min} is equal to the radius of the propeller as shown in Fig. 2(b). This distance can be decreased even further by adding an offset to the tilting axle, as shown in Fig. 2(c). Instead of being affected by the propeller size, D_{\min} mainly depends on the height of rotors h_{rotor} located closer to the wall. Thus, D_{\min} is greatly reduced. Furthermore, this configuration allows the usage of bigger propellers to increase the efficiency of propellers because the minimum distance, D_{\min} does not depend on the propeller size [15].

The proposed configuration, nevertheless, requires caution when perching and climbing on the wall, owing to the wall and ground effects [16]. According to the results of [16], the recirculation effect occurs when the propeller is close to the wall. Because of the recirculation effect, the rotor's thrust close to the wall decreases, and the platform rotates toward the wall and thus sticks. Although there are some experimental results [17], there is no clear modeling for this effect so far. By referring to the results of [17], we judged that the ceiling effect could be neglected if the rotor is located from the wall by more than 0.3 times the radius of the propeller. This was set to the minimum distance to be kept from the wall and was reflected in the platform design.

B. System Design

Fig. 1. shows the 3D CAD drawing and the prototype produced following design considerations in Section II-A. The appearance of the drawing and the prototype are slightly different, because of motion capture markers for pose estimation, a wall-contacting module for wall perching and climbing, and protective guards for safety. Detailed specifications of prototype components are described in Section V-A.

The CAROS-Q's tilting mechanism is shown in Fig. 3(a). A very simple tilting mechanism is adopted to reduce the weight and complexity. As a servo motor can rotate only one side, the idler and servo motor hinge frame are attached to the non-rotating side to rotate both sides. And then, the left and right tilting arms with two rotors each are connected to both sides of the servo motor. With this simple mechanism, CAROS-Q can rotate four rotors with only one servo motor.

We need to be careful when controlling the tilting angle. As observed in Fig. 3(b), the tilting angle α should not be less than zero so that the propellers do not collide with the wall during

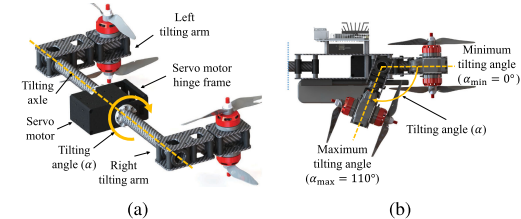


Fig. 3. (a) 3D CAD drawing of the CAROS-Q's tilting mechanism. (b) The side view of CAROS-Q. The tilting angle is constrained by one-way rotation to avoid collision with the wall.

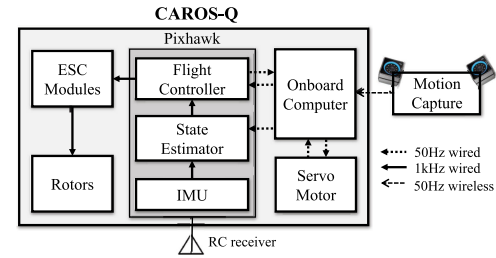


Fig. 4. The schematic diagram of the overall system setup. A motion capture system is used for an indoor pose estimation. The RC receiver receives user input from the RC controller.

wall climbing or perching. Therefore, the tilting angle is one-way constrained, and this constraint becomes a crucial issue for the controller. Likewise, the tilting servo motor exhibits a slow dynamics, owing to the additional torque induced from the rotor offset, which becomes another challenge. These two will be addressed further in Section IV.

The schematic diagram of the overall system including CAROS-Q is shown in Fig. 4. First, using wireless communication, the motion capture system transmits the pose measurement to the CAROS-Q’s onboard computer. And then, the onboard computer transmits the pose measurement to Pixhawk’s state estimator. With the Extended Kalman Filter (EKF), the state estimator estimates the linear velocity and pose by fusing the IMU and motion capture measurements. The estimated values, along with the user inputs received from the RC receiver, are then forwarded to the flight controller. The onboard computer then transmits the desired tilting angle transferred from the flight controller to the servo motor and receives the current tilting angle from the servo motor. In addition, the desired rotor speeds from the flight controller are fed into the ESC module, which then controls the rotors. The flight controller is described in more detail in Section IV.

III. MODELING

Fig. 5 shows the coordinate frame of CAROS-Q. $\{I\}$ denotes the global fixed frame or the inertial frame, and $\{B\}$ denotes the body frame located at the center of gravity of CAROS-Q. $\{A\}$ represents a frame rotated by a tilting angle α about the body frame's y -axis, and it is located at the center of the tilting axle.

Under the assumption that the platform is rigid and the tilting does not occur rapidly, the Newton-Euler formulation can be written as follows:

$$\begin{bmatrix} m\mathbf{I}_3 & 0 \\ 0 & \mathbf{J}(\alpha) \end{bmatrix} \begin{bmatrix} \dot{\mathbf{v}}^B \\ \dot{\omega}^B \end{bmatrix} + \begin{bmatrix} \boldsymbol{\omega}^B \times (m \cdot \mathbf{v}^B) \\ \boldsymbol{\omega}^B \times (\mathbf{J}(\alpha) \cdot \boldsymbol{\omega}^B) \end{bmatrix} = \begin{bmatrix} \mathbf{F}^B \\ \mathbf{M}^B \end{bmatrix} \quad (4)$$

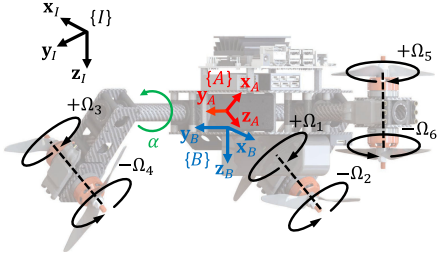


Fig. 5. Coordinate frames of CAROS-Q. $\{I\}$, $\{B\}$, and $\{A\}$ stand for inertial frame, body frame, and tiltable axle frame, respectively. Ω_i denotes the speed of the i -th rotor, which spins only in one direction. CAROS-Q is symmetrical about the $x_B z_B$ -plane.

where m is the mass of the whole platform, \mathbf{I}_3 the 3×3 identity matrix, $\mathbf{J}(\alpha)$ the inertial tensor which will be described in detail in this section, \mathbf{v} and $\boldsymbol{\omega}$ the linear / angular velocities, \mathbf{F} and \mathbf{M} the force and moment, respectively. The superscript B denotes that a value is expressed in the body frame. Under the assumption that the body does not move at high speed, the aerodynamic model can be written as if the thrust is proportional to the square of the number of rotations of the rotor.

Because of the rotor offset, a torque caused by the propellers is applied to the tilting axle along the body's y -axis. Also, the rotor offset increases the moment of inertia of the tilting arm. As a result, τ_{rot} , the induced torque applied to the body when accelerating the tilting arm, needs to be considered owing to the angular momentum conservation law. The torque can be compensated in the rate controller with the feed-forward input modeled from the following equation:

$$\tau_{\text{rot}} = k_m I_m \hat{\mathbf{y}}_B - \sum_1^4 (\mathbf{T}_i \times \mathbf{r}_i) + m_{\text{arm}} \mathbf{g} \times \mathbf{r}_{\text{arm}} \quad (5)$$

where k_m and I_m are the motor constant and applied current of the tilting servo motor, respectively, $\hat{\mathbf{y}}_B$ the unit vector of the body's y -axis, \mathbf{T}_i the i -th rotor's thrust force, \mathbf{r}_i the vector from the CoG to the i -th rotor, m_{arm} the mass of the arm part, and \mathbf{r}_{arm} the vector from the tilting axle to the tilting rotors.

The CoG of most multirotors is located at the geometric center of the platform, but that of CAROS-Q depends on the tilting angle, α . Likewise, the total inertial tensor, $\mathbf{J}(\alpha)$, depends on it. After calculating inertial tensors with reference to each part's CoG, the total inertial tensor can be calculated by using the parallel axis theorem as follows:

$$\begin{aligned} \mathbf{J}(\alpha) &= \mathbf{J}_{\text{body}} - m_{\text{body}} [\mathbf{r}_{\text{body}} - \mathbf{r}_{\text{CoG}}]_{\times}^2 \\ &\quad + \sum_1^4 (\mathbf{R}_y(\alpha) \mathbf{J}_{\text{rot}} \mathbf{R}_y^T(\alpha) - m_{\text{rot}} [\mathbf{r}_{\text{rot},i} - \mathbf{r}_{\text{CoG}}]_{\times}^2) \\ &\quad + \sum_5^6 (\mathbf{J}_{\text{rot}}(\alpha) - m_{\text{rot}} [\mathbf{r}_{\text{rot},i} - \mathbf{r}_{\text{CoG}}]_{\times}^2) \end{aligned} \quad (6)$$

where,

$$\begin{aligned} \mathbf{J}_{\text{body}} &= \frac{m_{\text{body}}}{12} \text{diag}(h_{\text{body}}^2 + w_{\text{body}}^2, \\ &\quad h_{\text{body}}^2 + l_{\text{body}}^2, w_{\text{body}}^2 + l_{\text{body}}^2)) \\ \mathbf{J}_{\text{rot}} &= \frac{m_{\text{rot}}}{12} \text{diag}(3r_{\text{rot}}^2 + h_{\text{rot}}^2, 3r_{\text{rot}}^2 + h_{\text{rot}}^2, 6r_{\text{rot}}^2) \\ \mathbf{r}_{\text{CoG}} &= \frac{m_{\text{body}} \mathbf{r}_{\text{body}} + \sum_1^6 m_{\text{rot}} \mathbf{r}_{\text{rot},i}}{m_{\text{body}} + 6m_{\text{rot}}} \end{aligned}$$

where \mathbf{J}_{body} is the inertial tensor of the body with reference to its own CoG, $\mathbf{J}_{\text{rot},i}(\alpha)$ the inertial tensor of the i -th rotor with reference to its own CoG, m_{rot} the mass of each rotor, m_{body} , h_{body} , w_{body} , l_{body} , and r_{body} the mass, height, width, length, and the radius of the body part, respectively, $\mathbf{r}_{\text{rot},i}$ the position vector of the i -th rotor from the inertial frame to the CoG, \mathbf{R}_y the rotation matrix about the body's y -axis, and $[\cdot]_{\times}$ the skew-symmetric matrix.

Based on this modeling, the force is analyzed in the body frame, and the following relationship is established:

$$\mathbf{F}^B = \mathbf{R}_A^B \left(\sum_{i=1}^4 \mathbf{T}_i^A \right) + \sum_{i=5}^6 \mathbf{T}_i^B \quad (7)$$

$$\mathbf{M}^B = \mathbf{R}_A^B \left(\sum_{i=1}^4 \boldsymbol{\tau}_i^A \right) + \sum_{i=5}^6 \boldsymbol{\tau}_i^B + \sum_{i=1}^6 (\mathbf{r}_{\text{rot},i} - \mathbf{r}_{\text{CoG}}) \times \mathbf{T}_i^B \quad (8)$$

where \mathbf{R}_A^B is the rotation matrix from $\{A\}$ to $\{B\}$. The mapping between the force, moment, tilting angle and rotor's rotational speed in the body frame can be expressed in the matrix form as follows:

$$\begin{bmatrix} \mathbf{F}_{xz}^B \\ \mathbf{M}^B \end{bmatrix} = \mathbf{A}(\alpha) \boldsymbol{\Omega} \quad (9)$$

where

$$\delta = \mu(l_0(1 + m_{\text{rate}}) + p_{0,x} c_{\alpha} + p_{0,z} s_{\alpha}),$$

$$\epsilon = \mu(p_{0,x} - l_2 - l_0 m_{\text{rate}} c_{\alpha}),$$

$$m_{\text{rate}} = \frac{4m_{\text{rot}}}{m_{\text{body}} + 6m_{\text{rot}}},$$

Ω_i is the speed of the i -th rotor, μ is the lift coefficient, κ is the drag coefficient, c_{α} denotes $\cos \alpha$, s_{α} denotes $\sin \alpha$, $\boldsymbol{\Omega} = [\Omega_1^2, \Omega_2^2, \dots, \Omega_6^2]^T$, $\mathbf{A}(\alpha) = \mathbb{R}^{5 \times 6}$ is the allocation matrix with respect to α , l_0 the distance between the tilting axle and rotors, l_1 half of the distance between the tilting rotors, and l_2 the distance between the tilting axle and the fixed rotors, as shown in Fig. 1. Furthermore, $p_{0,x}$ and $p_{0,z}$ are the x and z coordinate positions of the CoG, respectively, when the tilting angle is zero. \mathbf{F}_{xz}^B is a 2×1 force vector, which shall be described in Section IV.

$$\mathbf{A}(\alpha) = \begin{bmatrix} \mu s_{\alpha} & \mu s_{\alpha} & \mu s_{\alpha} & \mu s_{\alpha} & 0 & 0 \\ \mu c_{\alpha} & \mu c_{\alpha} & \mu c_{\alpha} & \mu c_{\alpha} & \mu & \mu \\ \kappa s_{\alpha} - \mu l_1 c_{\alpha} & -\mu l_1 c_{\alpha} - \kappa s_{\alpha} & \mu l_1 c_{\alpha} + \kappa s_{\alpha} & \mu l_1 c_{\alpha} - \kappa s_{\alpha} & 0 & 0 \\ \delta & \delta & \delta & \delta & \varepsilon & \varepsilon \\ -\kappa c_{\alpha} - l_1 \mu s_{\alpha} & \kappa c_{\alpha} - l_1 \mu s_{\alpha} & l_1 \mu s_{\alpha} - \kappa c_{\alpha} & \kappa c_{\alpha} + l_1 \mu s_{\alpha} & -\kappa & \kappa \end{bmatrix} \quad (10)$$

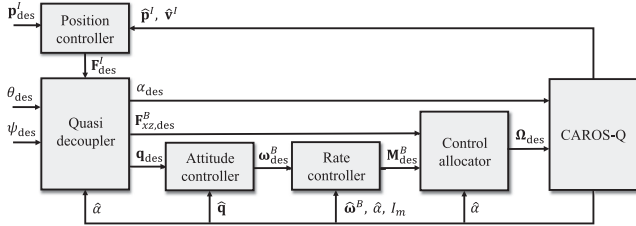


Fig. 6. The control diagram of CAROS-Q. The controller is running on the Pixhawk flight controller.

The allocation matrix of the conventional multirotor is static. A tilting multirotor such as CAROS-Q, nevertheless, does not have a static allocation matrix. The method to solve this problem is suggested in the control allocation part of the following section.

IV. CONTROL ARCHITECTURE

A. Control Diagram

Fig. 6 shows the overall control diagram of CAROS-Q. The desired position $\mathbf{p}_{\text{des}}^I$, expressed in the inertial frame with the superscript denoting the inertial frame, is fed to the position controller along with $\hat{\mathbf{p}}^I$ and $\hat{\mathbf{v}}^I$, where $\hat{\cdot}$ denotes estimated current value. After that, $\mathbf{F}_{\text{des}}^I$ is calculated and passed into the quasi-decoupler, which will be discussed later. This quasi-decoupler also takes in $\hat{\alpha}$ and the desired pitch θ_{des} and yaw ψ_{des} . Then, it outputs the desired tilting angle α_{des} , $\mathbf{F}_{xz,\text{des}}^B$, and the desired quaternion \mathbf{q}_{des} . Each output is sent to the CAROS-Q platform, the control allocator, and the attitude controller, respectively, in the abovementioned order. With \mathbf{q}_{des} , the attitude controller outputs the desired angular velocity ω_{des}^B using $\dot{\mathbf{q}}$. Then, ω_{des}^B is merged with $\dot{\omega}^B$ and I_m resulting in the desired moment $\mathbf{M}_{\text{des}}^B$. I_m is used to calculate the feed-forward torque compensation term. $\mathbf{F}_{xz,\text{des}}^B$ and $\mathbf{M}_{\text{des}}^B$ are fed to the control allocator to generate Ω_{des} . The least square method with an $\hat{\alpha}$ dependent allocation matrix $\mathbf{A}(\hat{\alpha})$ is used to calculate Ω_{des} .

B. Position Control

The position controller is composed of a PID controller with the gravity compensation term as follows:

$$\mathbf{F}_{\text{des}}^I = K_{p,p} \mathbf{p}_{\text{err}} + K_{d,p} \dot{\mathbf{p}}_{\text{err}} + K_{i,p} \int \mathbf{p}_{\text{err}} dt + mg \quad (11)$$

where $\mathbf{p}_{\text{err}} = \mathbf{p}_{\text{des}}^I - \hat{\mathbf{p}}^I$ and $K_{p,p}$, $K_{d,p}$, and $K_{i,p}$ are the proportional, derivative, and integral gains of the position controller, respectively.

C. Quasi-Decoupler

The platform has to orient its attitude while maintaining its position, which therefore means that it is imperative to have a decoupled system. Conventional tilting multirotor controllers decouple the originally coupled x -position and pitch-axis or y -position and roll-axis by generating the corresponding desired servo motor angle vector α_{des} and Ω_{des} through \mathbf{F}_{des} and \mathbf{M}_{des} from the controller. Generally, α_{des} will be a vector if we use multiple servo motors, but without loss of generality, we will use a scalar representation because we just have one servo motor in CAROS-Q. Thus, the response time and angular constraint of the

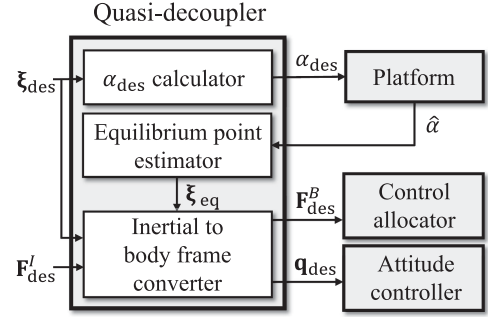


Fig. 7. The diagram of quasi-decoupler consisting of α_{des} calculator, equilibrium point estimator, and inertial to body frame converter.

tilting servo motor are important factors in controlling a tilting multirotor with conventional approaches [14], [15]. However, for the proposed platform, the servo motor, which is inevitably slower than the rotors, becomes even slower because of the additional torque owing to the rotor offset. Furthermore, the rotor offset limits the servo motor angle to avoid collision on the wall-climbing or perching phase. As a result, the conventional decoupling methods cannot be applied to CAROS-Q directly.

For this reason, we suggest a method, hereafter called quasi-decoupling, which solves the aforementioned problems at the same time. The proposed control method enables the change of orientation while maintaining position, regardless of the response time and angular constraint of the tilting servo motor. As shown in Fig. 7, quasi-decoupling is a three-step process. The detailed steps are as follows. First, the α_{des} calculator determines adequate α_{des} using $\mathbf{F}_{\text{des}}^I$ and ξ_{des} . Then, α_{des} is fed to the servo motor. Second, with $\hat{\alpha}$ from the servo motor, the equilibrium point estimator determines ξ_{eq} , the desired rotation that enables the platform to maintain an equilibrium point, where $\mathbf{F}^I = mg$ and $\mathbf{M}^B = 0$. Then, ξ_{eq} is fed to the inertial to body frame converter. Finally, the inertial to body frame converter calculates \mathbf{q}_{des} and converts $\mathbf{F}_{\text{des}}^I$ to \mathbf{F}_{xz}^B . Then, \mathbf{q}_{des} and \mathbf{F}_{xz}^B are fed to the attitude controller and the control allocator, respectively.

The difference between the conventional method and the proposed method is revealed in the following equation. The conventional tilting multirotor allocation method is described as follows:

$$\begin{bmatrix} \mathbf{F}_{\text{des}}^B \\ \mathbf{M}_{\text{des}}^B \end{bmatrix} = f(\alpha_{\text{des}}, \Omega_{\text{des}}). \quad (12)$$

For the conventional method, α_{des} and Ω_{des} are nonlinearly coupled. Therefore, the servo motor's response time and angular constraint are important for control. However, this is not the case in the proposed method, which is expressed as follows:

$$\begin{bmatrix} \mathbf{F}_{\text{des}}^B \\ \mathbf{M}_{\text{des}}^B \end{bmatrix} = f(\hat{\alpha}, \Omega_{\text{des}}) \quad (13)$$

where $\hat{\alpha}$ denotes the estimated current angle of the servo motor. For the proposed method, α_{des} and Ω_{des} are independent of each other. As such, with quasi-decoupling, the controller's performance becomes independent to the response time and angular constraint of the servo motor.

In summary, while the existing method controls the platform by simultaneously using a servo motor and the rotors to follow the desired force and moment input, the proposed method uses only the rotors. As a result, the orientation is adjustable without

altering the position despite the slow servo motor dynamics and angular constraint, which overcomes the conventional methods' limitations. Afterward, the position and yaw can be controlled using a conventional 4-DOF multirotor controller on the new equilibrium point.

The quasi-decoupling method has been implemented for the proposed platform to quasi-decouple the x -position and pitch-axis. For the proposed platform, the numbers of decoupling axes and servo motors are the same. Therefore, for a given desired attitude, there always is a unique solution that makes the platform maintain its equilibrium point if physically available. Thus, it is possible to calculate the solution without heavy computation, such as nonlinear least square optimization. Also, because CAROS-Q has only a single tilting axle, vectors α_{des} and $\hat{\alpha}$ can be simplified to 1×1 vectors $[\alpha_{1,\text{des}}]$ and $[\hat{\alpha}_1]$, respectively. Furthermore, ξ_{des} and ξ_{eq} become $\mathbf{R}_z(\psi_{\text{des}})\mathbf{R}_y(\theta_{\text{des}})$ and $\mathbf{R}_y(\theta_{\text{eq}})$, respectively.

To implement the method, the relationship between $\alpha_{1,\text{des}}$ and θ_{des} suitable for the platform configuration needs to be obtained. With the assumption that the platform is in the equilibrium point ($\mathbf{F}^I = mg$, $\mathbf{M}^B = 0$), equations (4) and (9) can be organized as a nonlinear system equation regarding F_x^B , F_z^B , and M_y^B . The relationship can be obtained by solving the following nonlinear system:

$$\begin{aligned} F_x^B : F_1 \sin(\alpha_{1,\text{des}}) &= \|\mathbf{F}^I\| \sin(\theta_{\text{des}}) \\ F_z^B : F_1 \cos(\alpha_{1,\text{des}}) + F_2 &= \|\mathbf{F}^I\| \cos(\theta_{\text{des}}) \\ M_y^B : F_1 \left(\left(\frac{m_{\text{body}}}{m_{\text{body}} + m_{\text{arm}}} \right) l_0 + h_t \sin(\alpha_{1,\text{des}}) + l_1 \cos(\alpha_{1,\text{des}}) \right) \right. \\ &\quad \left. - \left(l_2 - \left(l_1 - \frac{m_{\text{arm}}}{m_{\text{body}} + m_{\text{arm}}} l_0 \cos(\alpha_{1,\text{des}}) \right) \right) F_2 = 0 \end{aligned} \quad (14)$$

where $F_1 = \mu \sum_1^4 \Omega_i^2$ and $F_2 = \mu \sum_5^6 \Omega_i^2$.

Once (14) is solved, we can acquire $\alpha_{1,\text{des}}$, which enables the platform to hover for θ_{des} . The relationship is also valid with θ_{eq} and $\hat{\alpha}_1$. Using the equations obtained above and the relation between the rotation matrices, the output of the quasi-decoupler is obtained as follows:

$$\begin{aligned} \mathbf{R}_{\text{des}}^{IB} &= \mathbf{R}_z(\psi_{\text{des}})\mathbf{R}_{\text{thr}}\mathbf{R}_y(\theta_{\text{eq}}), \\ \mathbf{R}_{\text{thr}} &= \mathbf{I}_3 + [\hat{\mathbf{z}}_I \times \hat{\mathbf{F}}_{\text{des}}^I] \times \frac{1}{(1 + \hat{\mathbf{z}}_I \cdot \hat{\mathbf{F}}_{\text{des}}^I)} \\ &\quad + [\hat{\mathbf{z}}_I \times \hat{\mathbf{F}}_{\text{des}}^I] \times, \\ \mathbf{q}_{\text{des}} &= q_r + q_i \hat{\mathbf{i}} + q_j \hat{\mathbf{j}} + q_k \hat{\mathbf{k}}, \end{aligned} \quad (15)$$

where $\mathbf{R}_{\text{des}}^{IB}$ is the rotation matrix from the inertial frame to the body frame, $\mathbf{q}_{\text{des}} = (q_r, q_i, q_j, q_k)$, which can be obtained from the rotation matrix, as explained in [18], $\hat{\mathbf{F}}_{\text{des}}^I$ is the unit vector of $\mathbf{F}_{\text{des}}^I$, and \mathbf{R}_{thr} is the rotation matrix that rotates the unit vector $\hat{\mathbf{z}}_I$ onto the unit vector $\hat{\mathbf{F}}_{\text{des}}^I$. Finally, from (14), the desired output force \mathbf{F}_{xz}^B can be obtained as follows:

$$\mathbf{F}_{xz}^B = (\|\mathbf{F}_{\text{des}}^I\| \cdot \cos(\theta_{\text{eq}}), \|\mathbf{F}_{\text{des}}^I\| \cdot \sin(\theta_{\text{eq}}))^T. \quad (16)$$

As expressed in (10), the allocation matrix of CAROS-Q is a 5×6 matrix, unlike a normal hexarotor with a 4×6 matrix. Thus, $\mathbf{F}_{\text{des}}^I$ should be expressed only with F_x^B and F_z^B , which makes \mathbf{F}_{xz}^B a 2×1 vector.

TABLE I
CAROS-Q MAIN SPECIFICATIONS

Parameter	Value
Total weight	1.9 kg
Max. thrust of each BLDC motor [20]	14.2 N
Stall torque of XM540-W270-R [21]	10.60 Nm
Max. tilting angle	110°
Distance from tilting axle to tilting rotor	75 mm
Half of the distance between tilting rotors	135 mm
Distance from tilting axle to fixed rotor	220 mm

D. Attitude Control

The following attitude control method is based on [19]. The controller uses the quaternion error \mathbf{q}_{err} as follows:

$$\mathbf{q}_{\text{err}} = \mathbf{q}_{\text{des}} \otimes \hat{\mathbf{q}}^* = \begin{pmatrix} q_{w,\text{err}} \\ \mathbf{q}_{v,\text{err}} \end{pmatrix} \quad (17)$$

where $\hat{\mathbf{q}}^*$ is the conjugate of quaternion \mathbf{q} and \otimes is the Hamilton product. From the controller, ω_{des}^B can be calculated as follows:

$$\omega_{\text{des}}^B = K_q \text{sign}(q_{w,\text{err}}) \mathbf{q}_{v,\text{err}} \quad (18)$$

where K_q is the tuning parameter, $\text{sign}(\cdot)$ is the sign function, and $q_{w,\text{err}}$ and $\mathbf{q}_{v,\text{err}}$ are the scalar and vector parts of \mathbf{q}_{err} , respectively.

E. Rate Control

The rate controller is composed of a PD controller with the feedforward torque compensation term as follows:

$$\begin{aligned} \mathbf{M}_{\text{des}} &= \mathbf{J}(\hat{\alpha})(K_{p,r}\omega_{\text{err}} + K_{d,r}\dot{\omega}_{\text{err}}) + \hat{\omega} \times \mathbf{J}(\hat{\alpha})\hat{\omega} \\ &\quad + k_m I_m \hat{\mathbf{y}}_B - \sum_1^4 (\mathbf{T}_i \times \mathbf{r}_i) + m_{\text{arm}} \mathbf{g} \times \mathbf{r}_{\text{arm}} \end{aligned} \quad (19)$$

where $\omega_{\text{err}} = \omega_{\text{des}} - \hat{\omega}$, $K_{p,r}$ and $K_{d,r}$ are the proportional and derivative gains of the rate controller, respectively.

F. Control Allocator

The control allocation task is to calculate the corresponding rotor speeds for the given inputs $\mathbf{F}_{\text{des}}^B$ and $\mathbf{M}_{\text{des}}^B$. When the system is fully determined, meaning the system matrix has a full rank, the rotor speeds are determined using the matrix inverse. However, if the system is underdetermined, the pseudoinverse can be used to find the minimum-norm solution for the inputs. Thus, after receiving $\hat{\alpha}$ from the quasi-decoupler, the static allocation matrix is calculated and the least square solution is obtained as follows:

$$\boldsymbol{\Omega} = \mathbf{A}^\dagger(\hat{\alpha}) \begin{bmatrix} \mathbf{F}_{xz,\text{des}}^B \\ \mathbf{M}_{\text{des}}^B \end{bmatrix}$$

where $\mathbf{A}^\dagger(\hat{\alpha})$ is the pseudoinverse matrix calculated from the given $\hat{\alpha}$. As the system is underdetermined with six unknowns and five equations, the pseudoinverse gives the least square solution.

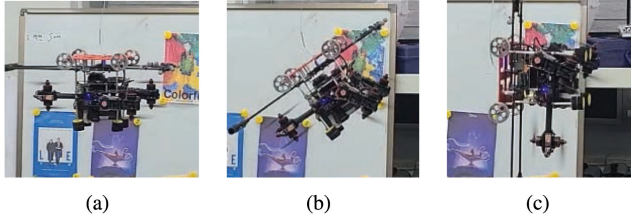


Fig. 8. CAROS-Q makes transition from 0° to 90° pitch angle while hovering. (a) After 3.5 s at 0° , (b) after 6.5 s at 45° , and (c) after 9 s at 90° .

V. PROTOTYPE AND EXPERIMENTS

A. Prototype Specification

The main electronic and mechanical components of the system are described in the following. To hold the platform's weight at a 90° pitch angle and rotate the tiltable axle, 5-in propellers, Xnova RM2207 2000KV motors [20], and Robotis Dynamixel XM540-W270-R [21] are used. Pixhawk4 mini [22] is used as a controller, and Jetson Nano [23] is utilized for an onboard computer. The main hardware parameters are shown in Table I.

B. Experimental Results

To validate proposed controller's performance, we performed two experiments. To obtain accurate ground truth location information, we used the OptiTrack Prime13 [24] motion tracker. Details of the experiments are as follows.

1) *Test I – Pitching While Hovering*: First, we evaluated the performance of the proposed controller during pitching while hovering. To check this, we pitched the platform between 0° and 90° while maintaining the position with the conventional and the proposed controllers. The platform failed to maintain the position while pitching with a conventional method. However, it was possible with the proposed method. Fig. 8 shows CAROS-Q while performing the test. As can be seen from the picture, the platform pitch up to 90° without significantly deviating from its original position during the pitching process. Fig. 9 shows the detailed log while performing the first test.

The pitch angle changes accordingly to $\hat{\alpha}$, to maintain the equilibrium point. As a result, the pitch angle has been changed without changing the position. There is a slight position error at 90° , which seems to be caused by errors between the actual platform and the model, and nonlinear aerodynamic effects caused by propeller interference. However, this error was less than 20 cm, which was an acceptable level, and the z -position error was removed through the z -position integral controller, taking 2 s. Another noteworthy thing is that the speeds of rotors 1, 3, and 5 located at the top are slower than the speeds of rotors 2, 4, and 6 located at the bottom (the rotor numbers are specified in Fig. 5). Owing to the characteristics of the coaxial platform, the lower rotors must rotate faster to generate the same amount of force because of the interference by the airflow generated from the upper rotor. In addition, as the pitch angle approaches 90° , the weight that first through fourth rotors located on the arm part must handle increases. As a result, the rotational speed of these rotors increases as the platform pitch angle approaches 90° .

2) *Test II – Wall Climbing*: We evaluated the CAROS-Q's wall-climbing performance in *Test II*. To minimize wall-reaction force and moment, the desired attitude was set to 90° , same as the inclined angle of the vertical wall. Fig. 10 shows the detailed sequence of the test. After pitching from the 0° hovering state,

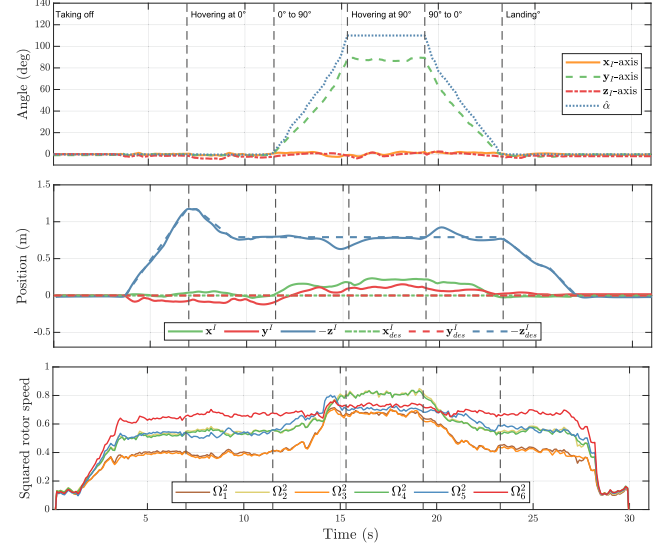


Fig. 9. (T-B): The orientation, position, and rotor speeds of CAROS-Q during *Test I*. The squared rotor speeds are scaled, with 1 representing the maximum thrust produced by a rotor. These results show that our proposed method enables the platform to pitch well while maintaining the x -position even though the servo motor is slow and one-way constrained.

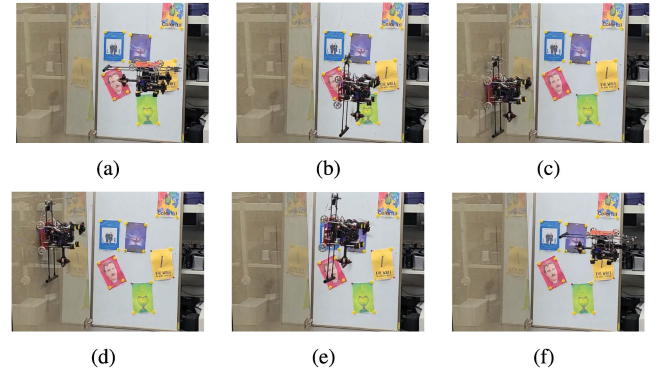


Fig. 10. A continuous motion of CAROS-Q performing the wall-climbing task. It proceeds in the order from (a) to (f). (a) After 17 s, (b) after 22 s, (c) after 28 s, (d) after 32 s, (e) after 36 s, and (f) after 40 s.

the platform perches, climbs, and detaches on the wall and then pitches back to 0° . Fig. 11 shows the detailed log during the process. First, for CAROS-Q to attach to the wall, pitching was performed from 0° to 90° from 18 s to 22 s, taking 4 s. The process shows the same behavior as *Test I*. From 22 s to 28 s, the platform moved about -0.6 m along x_I -axis at 90° while maintaining the other position to attach to the wall. As shown in Fig. 11, the platform's pitch angle is decreased to have a translation motion along x_I -axis, which indicates that the pitch-axis and x -position are successfully quasi-decoupled. From 28 s to 32 s, the platform climbed 0.4 m along the $-z_I$ -axis from 0.6 m to 1 m while attached to the wall. Thanks to the design considerations to reduce the wall effect, as described in Section II.A, the maneuvering behavior on the wall was almost the same as that in the air. From 32 s to 36 s, it shows the process of detaching from the wall. Afterward, the platform pitches back to 0° and lands. Through this experiment, we have shown that the proposed method showed promising results for midair pitching between 0° and 90° to wall climbing with only one servo motor, despite the servo motor's slow dynamics and angular constraint.

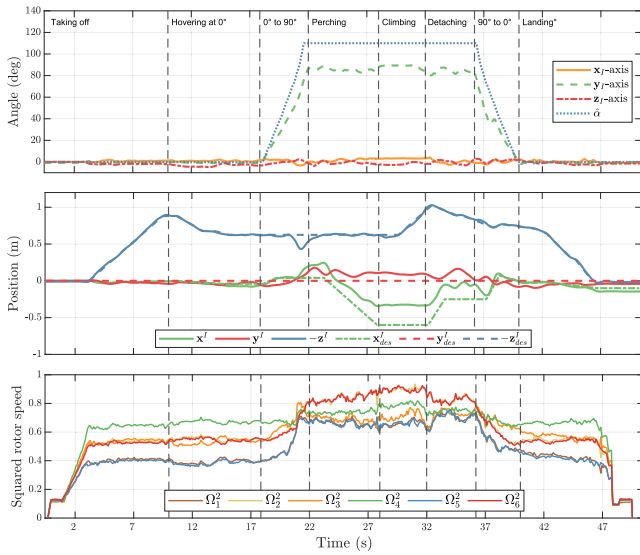


Fig. 11. (T-B): The orientation, position, and rotor speeds of CAROS-Q during *Test II*. The squared rotor speeds are scaled, with 1 representing the maximum thrust produced by a rotor. These results show that our method successfully quasi-decouples pitch-axis and x -position, performing the wall-climbing task without any difficulties.

A detailed video clip of all experiments is available at <https://youtu.be/pabRKNEwC14>.

VI. CONCLUSION

In this letter, we proposed a novel tilting multirotor called CAROS-Q, an optimized platform for wall-climbing tasks. Most tilting multirotors have a critical drawback in that they must maintain a certain distance from the wall. CAROS-Q solves this issue by adding rotor offsets to the tiltable axle, instead of placing the rotors directly on the axle. Furthermore, we analyzed the dynamics of CAROS-Q. We proposed a novel quasi-decoupler; it is a unique method that allows the platform to maintain the position while changing the orientation under the servo motor's slow dynamics and angular constraint. We verified the superior performance of the proposed controller through indoor experiments. Nevertheless, even though the proposed controller has proven successful when performing midair pitching and wall climbing, another controller needs to be designed to allow for accurate force control on the wall, which is our future work.

REFERENCES

- [1] H. Kim, B. Liu, C. Y. Goh, S. Lee, and H. Myung, "Robust vehicle localization using entropy-weighted particle filter-based data fusion of vertical and road intensity information for a large scale urban area," *IEEE Robot. Automat. Lett.*, vol. 2, no. 3, pp. 1518–1524, Jul. 2017.
- [2] S. Jung, S. Song, P. Youn, and H. Myung, "Multi-layer coverage path planner for autonomous structural inspection of high-rise structures," in *Proc. IEEE/RSJ Int'l Conf. Intell. Robots Syst.*, 2018, pp. 7397–7402.
- [3] S. M. Moon, C. Y. Shin, J. Huh, K. W. Oh, and D. Hong, "Window cleaning system with water circulation for building façade maintenance robot and its efficiency analysis," *Int'l J. Precis. Eng. Manuf.-Green Technol.*, vol. 2, no. 1, pp. 65–72, 2015.
- [4] B. Chu, K. Jung, C. S. Han, D. Hong, "A survey of climbing robots: Locomotion and adhesion," *Int'l J. Precis. Eng. Manuf.*, vol. 11, no. 4, pp. 633–647, 2010.
- [5] M. T. Pope *et al.*, "A multimodal robot for perching and climbing on vertical outdoor surfaces," *IEEE Trans. Robot.*, vol. 33, no. 1, pp. 38–48, Feb. 2017.
- [6] W. Myeong and H. Myung, "Development of a wall-climbing drone capable of vertical soft landing using a tilt-rotor mechanism," *IEEE Access*, vol. 7, pp. 4868–4879, 2018.
- [7] T. Ikeda *et al.*, "Wall contact by octo-rotor UAV with one DoF manipulator for bridge inspection," in *Proc. IEEE/RSJ Int'l Conf. Intell. Robots Syst.*, 2017, pp. 5122–5127.
- [8] S. Hamaza *et al.*, "Sensor installation and retrieval operations using an unmanned aerial manipulator," *IEEE Robot. Automat. Lett.*, vol. 4, no. 3, pp. 2793–2800, Jul. 2019.
- [9] M. Ryll, H. H. Bülthoff, and P. R. Giordano, "Modeling and control of a quadrotor UAV with tilting propellers," in *Proc. IEEE Int'l Conf. Robot. Automat.*, 2012, pp. 4606–4613.
- [10] M. Ryll, H. H. Bülthoff, and P. R. Giordano, "A novel overactuated quadrotor unmanned aerial vehicle: Modeling, control, and experimental validation," *IEEE Trans. Control Syst. Technol.*, vol. 23, no. 2, pp. 540–556, Mar. 2015.
- [11] P. Zheng, X. Tan, B. B. Kocer, E. Yang, and M. Kovac, "TiltDrone: A fully-actuated tilting quadrotor platform," *IEEE Robot. Automat. Lett.*, vol. 5, no. 4, pp. 6845–6852, Oct. 2020.
- [12] M. Ryll, D. Bicego, and A. Franchi, "Modeling and control of FAST-Hex: A fully-actuated by synchronized-tilting hexarotor," in *Proc. IEEE/RSJ Int'l Conf. Intell. Robots Syst.*, 2016, pp. 1689–1694.
- [13] A. Oosedo, S. Abiko, S. Narasaki, A. Kuno, A. Konno, and M. Uchiyama, "Flight control systems of a quad tilt rotor unmanned aerial vehicle for a large attitude change," in *Proc. IEEE Int'l Conf. Robot. Automat.*, 2015, pp. 2326–2331.
- [14] M. Kamel *et al.*, "The voliro omniorientational hexacopter: An agile and maneuverable tiltable-rotor aerial vehicle," *IEEE Robot. Automat. Mag.*, vol. 25, no. 4, pp. 34–44, Dec. 2018.
- [15] Y. Qin, W. Xu, A. Lee, and F. Zhang, "Gemini: A compact yet efficient bi-copter UAV for indoor applications," *IEEE Robot. Automat. Lett.*, vol. 5, no. 2, pp. 3213–3220, Apr. 2020.
- [16] E. B. Davis, "Aerodynamic force interactions and measurements for micro quadrotors," Ph.D thesis, Univ. Queensland: Australia, 2018.
- [17] B. B. Kocer, T. Tjahjowidodo, and G. G. L. Seet, "Centralized predictive ceiling interaction control of quadrotor VTOL UAV," *Aerospace Sci. Technol.*, vol. 76, pp. 455–465, 2018.
- [18] N. Trawny and S. I. Roumeliotis, "Indirect Kalman filter for 3D attitude estimation," Univ. Minnesota, Dept. Comp. Sci. Eng., Tech. Rep. 2005-002, vol. 2, 2005.
- [19] B. Dario, M. Hehn, and R. D'Andrea, "Nonlinear quadrocopter attitude control," Dep. of Mechanical and Process Eng., Tech. Rep. ETH Zurich, 2013.
- [20] "Xnova hypersonic RM2207-2000KV specifications," *Xnova Official Store*, Accessed: Apr. 15, 2021. [Online]. Available: <https://www.xnovamotors.com/xnova-hypersonic-rm2207-2000kv-specifications/>
- [21] "XM540-W270-T/R specifications," *ROBOTIS e-Manual*, Korea, Accessed: Apr. 15, 2021. [Online]. Available: <http://emanual.robotis.com/docs/en/dxl/x/xm540-w270/>
- [22] "Pixhawk4 mini," *Holybro Store*, Accessed: Apr. 15, 2021. [Online]. Available: https://shop.holybro.com/pixhawk4-mini_p1120.html
- [23] D. Franklin, "Jetson nano brings AI computing to everyone," *NVIDIA Developer Blog.*, Accessed: Apr. 15, 2021. [Online]. Available: <https://devblogs.nvidia.com/jetson-nano-ai-computing/>
- [24] "Prime^(x) 13 - Specs," *OptiTrack*, Accessed: Apr. 15, 2021. [Online]. Available: <https://optitrack.com/products/primex-13/specs.html>